Available online at www.sciencedirect.com

ScienceDirect

Journal of the European Ceramic Society 35 (2015) 1263–1271

www.elsevier.com/locate/jeurceramsoc

Size effect of thermal shock crack patterns in ceramics and numerical predictions

Xiaofeng Wu [a], Chiping Jiang [a,b], Fan Song [b,*], Jia Li [c], Yingfeng Shao [b], Xianghong Xu [b], Peng Yan [a]

[a] School of Aeronautic Science and Engineering, Beihang University, Beijing 100191, People's Republic of China
[b] State Key Laboratory of Nonlinear Mechanics, Institute of Mechanics, Chinese Academy of Sciences, Beijing 100190, People's Republic of China
[c] LSPM, CNRS UPR 3407, Université Paris XIII, 99 Avenue Jean-Baptiste Clément, Villetaneuse 93430, France

Received 17 June 2014; accepted 29 October 2014
Available online 16 November 2014

Abstract

The present work examines the size effect of thermal shock crack patterns in ceramics and develops quantitative predictions. A set of water-quenching experiments on thin ceramic specimens of different widths yielded two-dimensional, periodic and hierarchical readings of thermal shock crack patterns, which showed the strong size-dependence of the crack length and length hierarchy, and the size-independence of the crack spacing. Furthermore, the effective convective heat transfer coefficients inversely estimated from the crack spacing data were observed to be size-independent. Such a finding may help engineers to assess the thermal shock failure of practical ceramic components by designing specimens of standard size. Numerical simulations were conducted and the results are in good agreement with experimental data. Several interesting phenomena of the evolution of thermal shock crack patterns were revealed and discussed. The present study has led to a much improved scientific understanding of thermal shock cracking phenomenon of ceramics.
© 2014 Elsevier Ltd. All rights reserved.

Keywords: Ceramics; Thermal shock; Crack patterns; Numerical simulations; Size effect

1. Introduction

The excellent high temperature mechanical performance makes ceramic materials be widely used in the frontier fields of aerospace, power generation, and engine et al. However, the inherent brittleness of ceramic materials makes them particularly susceptible to thermal shock failure, even catastrophic fracture. The high temperature application of ceramics is an example that technique has largely preceded scientific understanding. It is recognized that a basic understanding of thermal shock failure must be gained to give full play to the potential of ceramic materials at high temperatures.[1]

Numerous studies on the thermal shock failure of ceramics have been conducted. Kingery[2] studied the thermal shock resistance of ceramic material and proposed the critical stress fracture theory based on the thermo-elastic stress analysis. Hasselman[3] proposed the thermal shock damage theory from the viewpoint of energy, and soon afterwards he[4] developed a unified theory of thermal shock fracture initiation and crack propagation in brittle ceramics. Lu and Fleck[5] analyzed the thermal shock resistance of brittle solids using a stress-based fracture criterion for a plate containing a distribution of flaws. Collin and Rowcliffe[6] studied the thermal shock behavior of brittle materials using the indentation quench method, obtained crack growth vs. temperature curves, and derived an expression for predicting the thermal shock resistance.

The thermal shock resistance of ceramic materials is affected by many factors, including quench medium,[7–9] porosity,[10,11] surface roughness,[12] specimen size,[13–22] and so on. Among them, the size effect attracted many researchers' attentions. Hasselman[13] theoretically indicated that strength of rods after thermal shock is inversely proportional to the 1/4 power of the

* Corresponding author. Tel.: +86 10 8254 3961; fax: +86 10 8254 3935.
E-mail address: songf@lnm.imech.ac.cn (F. Song).

http://dx.doi.org/10.1016/j.jeurceramsoc.2014.10.032
0955-2219/© 2014 Elsevier Ltd. All rights reserved.

rod diameter, and this conclusion was supported by experimental data for two rod sizes. Becher et al.[14] pointed out that at extreme of large specimen size (thickness > 4 mm), the values of critical thermal shock temperature difference become insensitive to size, while for small specimens, the effects of specimen size on thermal shock resistance, namely critical thermal shock temperature difference, are significant. Furthermore, Becher[15] pointed out that for room-temperature water quenching, the rapid increase in heat transfer coefficient as temperature overrides any changes in other factors, including specimen size; by raising the quench water temperature to 100 °C, a strong size dependence of critical temperature difference for small sizes was observed experimentally. Many studies on various materials revealed that the critical temperature difference[16,17] and the residual strength[16,18–22] after thermal shock decreases with the increase of specimen size.

The crack is the primary cause for the degradation of the strength in ceramic materials subjected to thermal shock. Researchers very early noticed that thermal shock cracks exhibit generally regular and elegant patterns, such as periodic and hierarchical characteristics, which are of practical importance for a clear understanding of the thermal shock failure mechanism of ceramics. Bažant[23] and Nemat-Nasser et al.[24,25] studied the stability of propagated thermal shock cracks (or drying shrinkage cracks) using the energy principle, and they theoretically discussed the length hierarchy phenomenon. Bahr et al.[26–28] established a fracture-mechanical model based on the time-dependent energy release rate to explain the thermal shock behaviors. Jenkins[29] used a method based on energy minimization to determine the spacing and penetration of a regular array of cracks in a shrinking slab due to a changing temperature field. Choules et al.[30] studied the thermal fracture of ceramic thermal barrier coatings and indicated the variations in crack patterns with the coating thickness and the thermal shock temperature.

In above mentioned studies, no quantitative predictions were reported. One of the challenging difficulties is the lack of accurate data on material properties at high temperatures. The dispersion of the available data[7,15,31,32] on the heat transfer coefficient is high up to one order magnitude. To overcome this difficulty and to bridge the gap between theoretical prediction and experimental data, Jiang et al.[33] developed a semi-inverse method, where the effective heat transfer coefficient (a quantity difficult to measure) was inversely estimated by the crack spacing (a quantity easy to measure), and predicted successfully the crack length and length hierarchy using a periodic assumption. Further, Li et al.[34] proposed a non-local failure model to simulate the thermal shock crack evolution. On the basis of the variational model to fracture developed by Francfort et al.[35,36], Bourdin[37,38], Sicsic[39], and Cyron[40] et al. conducted numerical studies for fracture analysis induced by thermal shock. These recent works verified and complemented each other, much promoted the studies on thermal shock cracking phenomenon of ceramics.

The purpose of the present work is to examine the size effect of thermal shock crack patterns in ceramics and to develop quantitative numerical predictions. This is not only to gain a better understanding of thermal shock cracking phenomenon of ceramics, but also to help engineers to assess the thermal shock failure of practical ceramic components using specimens of standard size.

2. Experimental

2.1. Experimental procedure

An experimental study was conducted to quantitatively observe the size effect of the crack patterns in ceramics after thermal shock by conventional water-quenching technique. 99% Al_2O_3 ceramic block (Xiongdi Material Co., Jiyuan, China) was cut into thin specimens with dimensions of $50 \times 2L \times 1\ mm^3$, where the half specimen width L ranges from 5 to 10 mm. Then the specimens were polished and tightly stacked together in sets of four, with four thick ceramic plates (5 mm in thickness) on the outside to prevent the temperature distribution from being disturbed by coolant accessing the interior surfaces of the specimens, as shown in Fig. 1. Thus only the two opposite long edges of the specimens were exposed to the coolant. To ensure thermal insulation, the other four faces of the specimen stack were twined by asbestos thread. Finally, the stacks of alumina plates were bound with inconel wires positioned 3–4 mm from the ends of the specimens.

The bound specimens were heated in a furnace at a rate of 10 °C/min to the preset temperature T_0 and maintained at this temperature for 20 min. From previous experiments,[33] it was observed that thermal shock crack patterns varied dramatically and the heat transfer coefficient reached its peak between $T_0 = 300$ °C and $T_0 = 400$ °C, so the values of T_0 were taken as 300, 350, and 400 °C. After heating, the heated specimens were dropped into a water bath at $T_1 = 15$ °C by free fall. The specimens were removed from the water bath 10 min later and dried, then dyed with blue ink to observe the cracks formed. Two sets of specimens (8 specimens in total) were tested at every value of T_0 and for every value of L to estimate the dispersion of experimental data.

2.2. Experimental results

The digitally scanned photographs of dyed specimens are shown in Fig. 2. It was observed that the thermal shock cracks were perpendicular to the top or bottom face, and the crack patterns on both of the sides of the specimen were identical, which showed that that the crack geometry was two-dimensional and convenient to observe and measure.

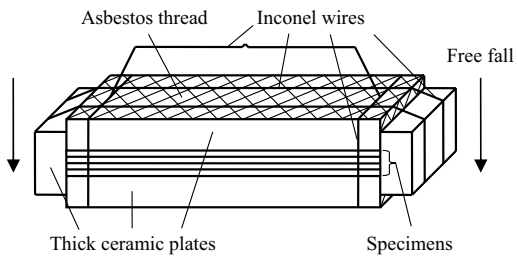

Fig. 1. Bound specimens for thermal shock, where the cross hatch represent the asbestos thread.

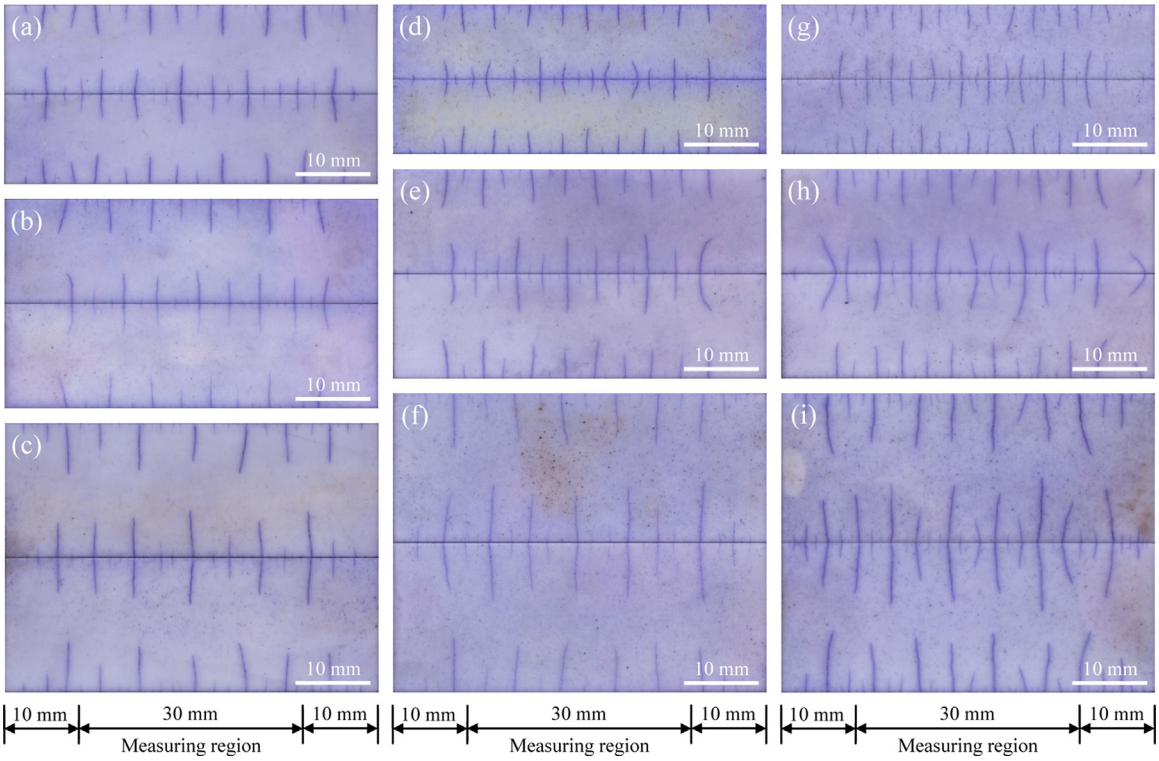

Fig. 2. Thermal shock crack patterns, where the half specimen width L = (a) 6 mm, (b) 7 mm, (c) 9 mm at preset temperature T_0 = 300 °C; L = (d) 5 mm, (e) 7 mm, (f) 10 mm at T_0 = 350 °C; L = (g) 5 mm, (h) 7 mm, (i) 10 mm at T_0 = 400 °C.

In measuring the geometry of the cracks, to remove the effects of the end boundaries, the regions within 10 mm from two ends of the specimens were excluded as shown in Fig. 2. The experiments showed that for the same specimen size, the higher the preset temperature T_0, the smaller the crack spacing. In addition, the long cracks became longer, while the short cracks became shorter as T_0 increased. These observations are in agreement with the previous experiments,[33] where only one single specimen size was used.

The experiments focus on the size effect of thermal shock crack patterns. In a statistical sense, four interesting variation laws of crack patterns with specimen size were found: (1) The crack length distribution exhibited elegant periodic and hierarchical characteristics at every preset temperature and for every specimen width. (2) The hierarchical number of crack length exhibited an increasing trend with the increase of the specimen width. Moreover, the wider the specimen, the longer the cracks of the longest level. However, the length of the cracks of other levels remained unchanged. (3) The spacing of the cracks of the longest level increased with the increase of specimen width, whereas the spacing of all the cracks was independent of the specimen width. (4) The fluctuation in the average crack spacing, s_0, in eight specimens at every value of the preset temperature T_0 and for every value of the half width L was very small, and the maximum standard deviation from the average value was less than 10%. The average crack spacing s_0 and corresponding standard deviation in eight specimens at various values of the preset temperature T_0 and for various values of the half width L are listed in Table 1.

How to interpret these variation laws of thermal shock crack patterns with the specimen width, and whether we can conduct a quantitative prediction, these will be studied in the following sections.

3. Numerical predictions

3.1. Theoretical considerations

According to the experimental observations, three simplified assumptions were made: (1) The cracks are two-dimensional, and are perpendicular to the boundary. (2) The crack patterns are hierarchical and periodic, consequently which can be simulated by a periodic unit. (3) From the assumption (1), the temperature

Table 1
Average crack spacing s_0 and corresponding standard deviation in eight specimens at various values of the preset temperature T_0 and for various values of the half width L.

T_0 (°C)	L (mm)	s_0 (mm)
300	6	1.579 ± 0.176
	7	1.570 ± 0.128
	9	1.563 ± 0.156
350	5	1.211 ± 0.105
	7	1.232 ± 0.035
	10	1.263 ± 0.113
400	5	1.045 ± 0.094
	7	1.006 ± 0.081
	10	1.035 ± 0.078

Table 2
Young's modulus E, Poisson's ratio ν, the mass density ρ, and the surface energy density γ of 99% Al_2O_3 ceramics, which are approximately independent of temperature. The data are provided by Xiongdi Material Co., Jiyuan, China.

E (GPa)	ν	ρ (kg/m^3)	γ (J/m^2)
323	0.22	3880	17.89

field is not disturbed by the cracks and remains one-dimensional. It can easily be calculated by Fourier's law of heat conduction. According to these assumptions, the thermal stress-strain field was determined by numerical method.

The numerical simulation of the thermal shock crack patterns is based on the minimum potential energy principle, namely optimal crack patterns minimize the average total potential energy density $\bar{W}$:

$$\bar{W}(s, p, t) = \frac{W(s, p, t)}{V} = \frac{U(s, p, t) + S}{V} = \frac{U(s, p, t) + \gamma pb}{V} \quad (1)$$

where s is the crack spacing, p is the crack length, t is the time, V is the volume of the computational unit, U is the strain energy, $S = \gamma pb$ is the crack surface energy (the energy required to form new crack surfaces) and γ is the surface energy density, b is the thickness of computational model.

Computations show that when the preset initial temperature of the specimen is less than the critical temperature ($T_0 < T_c$), the minimum value of $\bar{W}$ is located at $p = 0$, which indicates there is no thermal shock crack initiation; however, when $T_0 > T_c$ and after a very short time, the minimum value shifts to a location where both p and s become positive finite values, which indicates that cracks initiate. Both p and s change with time t, and the crack spacing s rapidly reaches a minimum s_0 due to the appearance of additional cracks. Then both p and s increase continuously with time t theoretically. However, considering the irreversibility of crack growth, the formed cracks will not recede or disappear, so the practical cracks will propagate while maintaining the constant spacing s_0, until the minimum point of $\bar{W}$ jumps to a curve representing "spatial period doubling", i.e. every second crack continues to propagate, whereas the other cracks stop. The process can be repeated and forms a hierarchical crack pattern.[33]

3.2. Computational region and material properties

The finite element software ANSYS was used for the numerical simulations. Noting the symmetry, first a quarter of a periodic unit was taken as the computational region, seeing the rectangle DOABC in Fig. 3(a), where O is the crack tip, u_x and u_z are the displacement components. When "spatial period doubling" appeared, the computational region was extended as the rectangle $DOABEO_0FC$ in Fig. 3(b), where O_0 and O are stationary and propagating crack tips, respectively.

The mechanical parameters such as Young's modulus E, Poisson's ratio ν, the mass density ρ, and the surface energy density γ of the material remain approximately unchanged in the range 0–600 °C, which are listed in Table 2. The coefficient of thermal

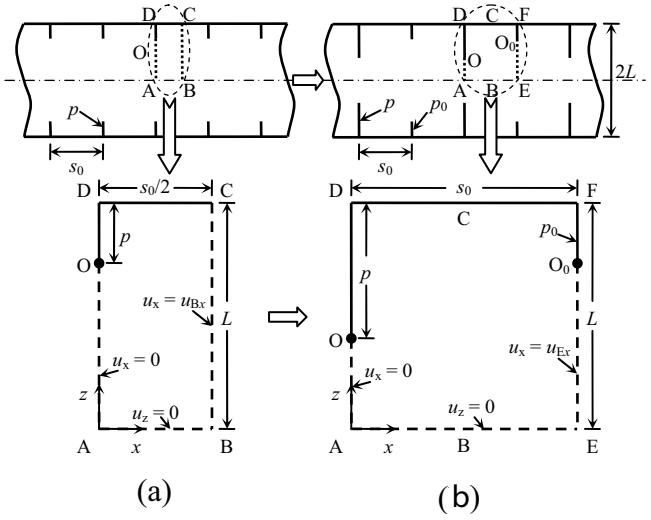

Fig. 3. Computational region and boundary conditions: (a) initial region, (b) extended region after crack hierarchy appears, where O_0F and OD represent, respectively, the propagating and stationary cracks, and dashed lines represent the symmetric boundaries cut from periodic unit.

expansion α, the thermal conductivity k and the specific heat c are strongly temperature-dependent, which are shown in Fig. 4.

One of the biggest challenges in numerical simulations arises from the lack of accurate data on the convective heat transfer coefficient h in thermal shock. To overcome this difficulty, we developed a semi-inverse method,[33] where the effective convective heat transfer coefficient $\bar{h}$ is inversely estimated from thermal shock crack spacing which is easily measured from experiments. Using the data of the crack spacing listed in Table 1, the estimated values of $\bar{h}$ at various values of T_0 and for various values of L are shown in Table 3. It can be observed that the variation tendency of $\bar{h}$ is in agreement with the existing data.[7,15,31–33]

From Table 3, it is observed that at the same T_0, the variations in the effective heat transfer coefficient $\bar{h}$ with the half width L are very small, so the size-independence of $\bar{h}$ can be assumed, i.e. under the experimental conditions in Fig. 1, $\bar{h}$ is not affected by the specimen width. Such a finding is of practical importance because it indicates that we can use the data of $\bar{h}$ estimated by experiments of one size specimens to predict the crack patterns of other size specimens, hence experimental effort can be greatly reduced. In the present numerical simulations, we used

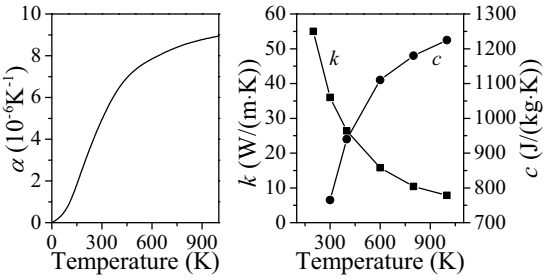

Fig. 4. Graphs of the thermal conductivity k,[41] the specific heat c,[42] and the coefficient of thermal expansion α[43] of 99% Al_2O_3 ceramics vs. temperature.

Table 3
Effective heat transfer coefficient $\bar{h}$ estimated by semi-inverse method at various values of T_0 and for various values of L.

T_0 (°C)	L (mm)	$\bar{h}$ (W/(m^2 K))
300	6	91,000
	7	90,500
	9	93,500
350	5	101,500
	7	99,000
	10	96,500
400	5	87,000
	7	89,500
	10	88,000

the effective heat transfer coefficients estimated by the specimens of $L = 7$ mm, i.e. $\bar{h}$ = 90,500, 99,000, 89,500 W/(m^2 K) at $T_0 = 300$, 350, 400 °C, respectively.

3.3. Numerical predictions and a comparison with experimental results

3.3.1. Size-dependence of crack spacing

Numerical results showed hierarchical characteristics of crack patterns. It is interesting to notice that if the specimen width is not very small (in the present computations, the half width $L \geq 2.5$ mm), the crack spacing of the shortest level is size-independent (apparently, the spacing, s_0, of all the cracks is also size-independent), whereas the crack spacing of the longest level is size-dependent. The variations in the crack spacing s_0 with the half width L at three values of T_0 are shown in Fig. 5, where the curves represent the numerical predictions and the points with error bar denote experimental data. In these simulations, the values of $\bar{h}$ were estimated by using the experimental data on the specimens of $L = 7$ mm. It should be pointed out that when the specimen width is very small, computations showed that no crack appears in specimens. Such results are in agreement with previous numerous studies.[13–22]

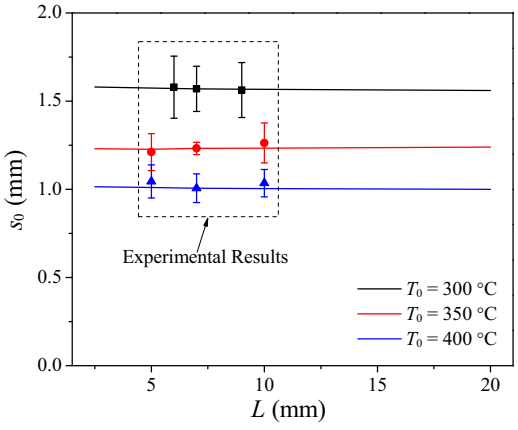

Fig. 5. Variations in the crack spacing s_0 with the half width L at three values of T_0, where the curves represent the numerical predictions and the points with error bar denote experimental data.

3.3.2. Size-dependence of crack length hierarchy

The penetration of thermal shock cracks plays a critical role in failure assessment of ceramic components. Numerical simulations showed that the hierarchical number of crack lengths increases with the increase of the specimen width. The column charts of computational values of the various level crack lengths p versus the half specimen width L at three values of the preset temperature T_0 are shown in Fig. 6, where crack length levels were arranged from short to long. From the theoretical considerations in Section 3.1, the ratio of the crack number of a two-level crack pattern is 1:1, it is 2:1:1 for a three-level crack pattern and 4:2:1:1 for a four-level crack pattern. Due to random factors, experimental data exhibited some degree of dispersity. According to the above ratios, the experimental statistical results of the thermal shock crack length in Fig. 2 were classified and depicted in Fig. 6 by points with error bar. It can be seen that the numerical predictions are in good agreement with experimental results. Obviously the theoretical considerations and numerical simulations can help to capture the essential characteristics of thermal crack patterns.

From Figs. 6 and 2, it is found that the length of the longest cracks considerably increases with the specimen width, which indicates that the increase of the specimen width can not necessarily improve strength.

4. Discussions

In this section an attempt is made to better understand the formation mechanics of above mentioned crack patterns from the angle of the thermal stress and energy.

4.1. Thermal stress and strain energy at crack initiation

Why does the crack spacing s_0 remain size-independent? Let us examine the distribution of the thermal stress and strain energy at crack initiation. In the present numerical simulations the time of crack initiation is about $t = 0.01$ s. From the present experiments shown in Fig. 1, the decisive stress is the x-directional stress σ_x. Assuming no crack appears at $t = 0.01$ s, the distributions of σ_x and the strain energy density U_0 along z-direction (the distance from the thermal shock surface) at $T_0 = 350$ °C for various values of the half width L are shown in Fig. 7. It is seen that when $L \geq 2.5$ mm, the distributions of σ_x and U_0 near the surface can be regarded as size-independent, thus the crack spacing s_0 determined by σ_x and U_0 can also be regarded as size-independent.

The distributions of the x-directional stress σ_x and the strain energy density U_0 along z-direction for $L = 7$ mm at $t = 0.01$ s and various values of the preset temperature T_0 are shown in Fig. 8. It is seen that σ_x and U_0 near the surface increase with the increase of T_0. This fact explains the phenomenon that the higher the preset temperature T_0, the smaller the crack spacing.

4.2. Crack pattern evolution and total potential energy

Section 4.1 shows that the distributions of the thermal stress and strain energy at crack initiation are independent of the

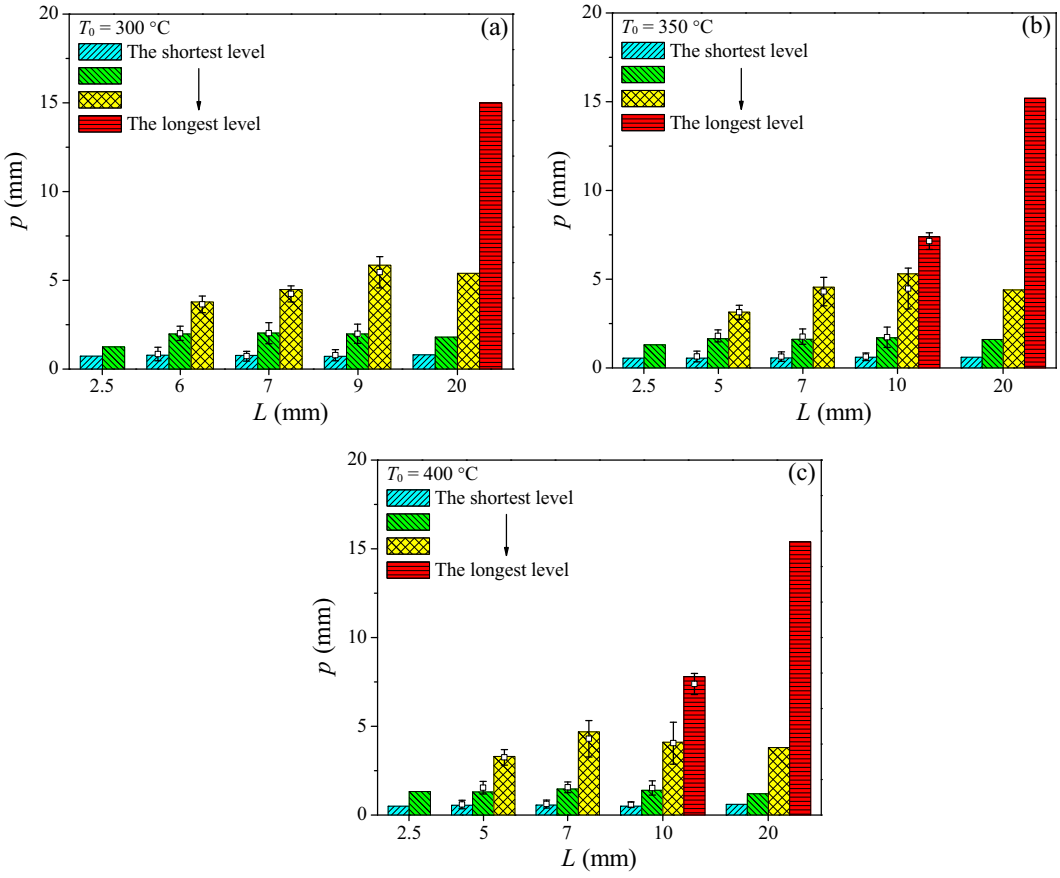

Fig. 6. Numerical predictions of various level crack lengths p versus the half specimen width L at three values of the preset temperature T_0. The corresponding classified experimental results are also shown by points with error bar.

specimen width $2L$ when $L \geq 2.5$ mm. Now we discuss the relation of the crack pattern evolution to the total potential energy W (refer to Eq.1) during crack propagation.

As an example, the evolution of the crack spacing s, crack length p as well as the total potential energy W with time t is shown in Fig. 9, where $T_0 = 350$ °C, $L = 2.5$, 7, and 10 mm, t_1, t_2, t_3 represent the time points corresponding to the "spatial period doubling" of the crack spacing, and W denotes the total potential energy stored in the 30 mm measuring region of the specimens as shown in Fig. 2.

The driving force of thermal shock crack propagation is provided by the total potential energy W. It can be seen from Fig. 9 that W first increases and goes up to its maximum, then decreases. At the stage where W increases, there are several characteristic time points t_1, t_2, ... when "spatial period doubling"

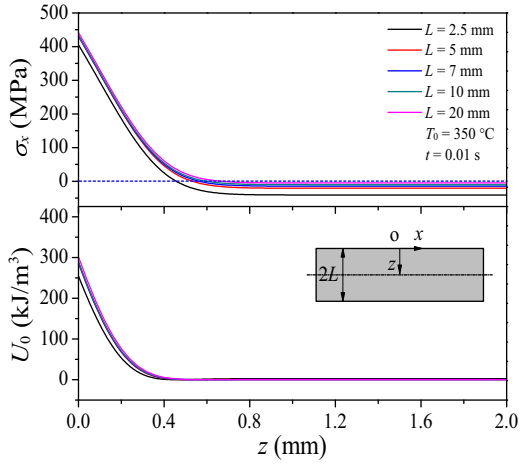

Fig. 7. Distributions of the thermal stress σ_x and the strain energy density U_0 along z-direction at $T_0 = 350$ °C and $t = 0.01$ s for various values of the half width L.

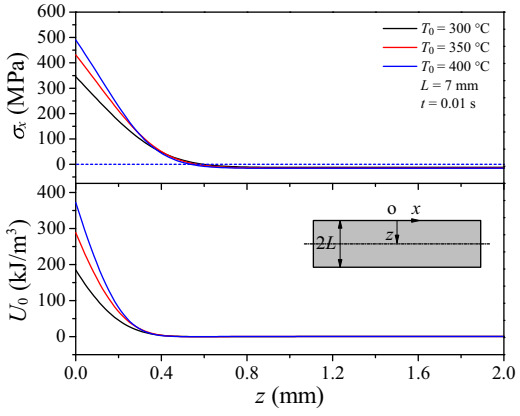

Fig. 8. Distributions of the thermal stress σ_x and the strain energy density U_0 along z-direction for $L = 7$ mm at $t = 0.01$ s and various values of the preset temperature T_0.

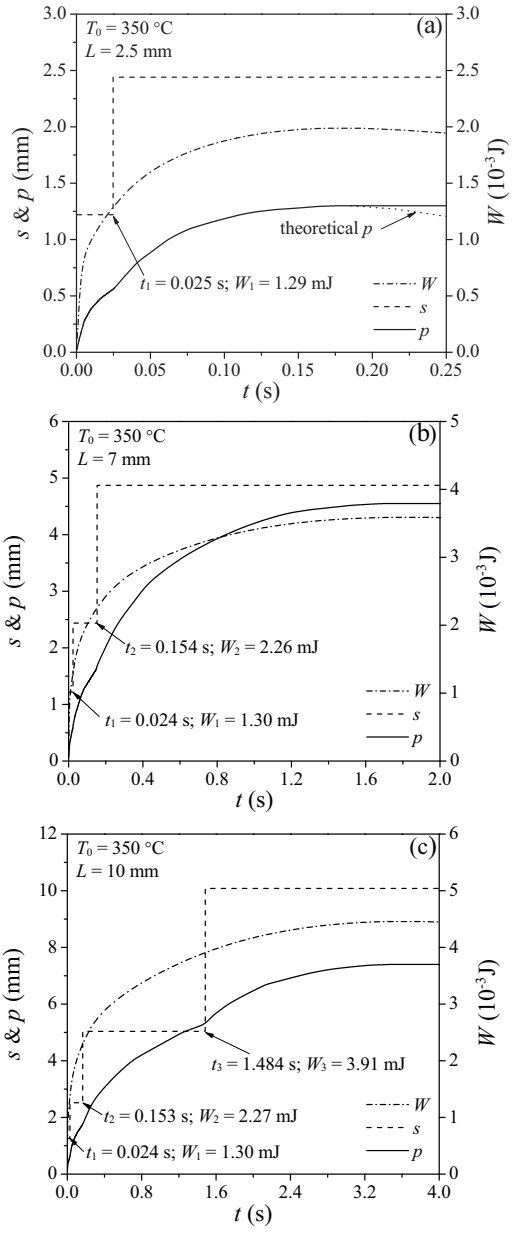

Fig. 9. Evolution of the crack spacing s, crack length p as well as the total potential energy W with time t at $T_0 = 350\,^{\circ}C$ for $L = 2.5$, 7 and 10 mm, where t_1, t_2, t_3 represent the time points corresponding to the "spatial period doubling" of the crack spacing, and W denotes the total potential energy stored in the 30 mm measuring region of the specimens as shown in Fig. 2.

of the crack spacing occurs, i.e. every second crack continues to propagate, whereas the other cracks stop. Fig. 9 shows that at these time points the crack propagation speed shows a sudden increase as the strain energy supports propagation of only half of the cracks. At the stage where W decreases, the idealized crack length p should decrease as shown by the dotted line in Fig. 9(a), however, the cracks formed do not recede or disappear, so the practical crack length remains unchanged.

For the convenience of comparison, the total potential energy W versus time t extracted from Fig. 9(a)–(c) is redrawn in Fig. 10 at $T_0 = 350\,^{\circ}C$ for $L = 2.5$, 7 and 10 mm, respectively. It is especially interesting to notice from Figs. 9 and 10 that

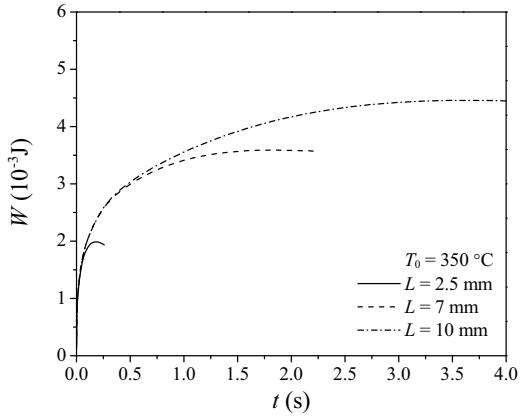

Fig. 10. Total potential energy W versus time t at $T_0 = 350\,^{\circ}C$ for $L = 2.5$, 7 and 10 mm, respectively.

before the cracks of the longest level propagate alone (the other cracks stop), the curves of the total potential energy W coincide almost with each other for specimens of different widths. This fact implies a theoretical inference that except the cracks of the longest level, the crack lengths of various levels and the corresponding time points of "spatial period doubling" of the crack spacing should be size-independent. The former part of the inference can be verified by experimental data as well as by numerical predictions. From Fig. 6, it can be seen that except the cracks of the longest level, the crack lengths of the corresponding levels for specimens of different widths are almost equal, where the column charts denote the numerical predictions and the points with error bar denote the experimental data. The latter part of the inference is verified by the numerical simulations. From Fig. 9(a)–(c), it can be seen that the first characteristic time point of "spatial period doubling" $t_1 = 0.025$, 0.024, 0.024 s and the corresponding total potential energy $W_1 = 1.29$, 1.30, 1.30 mJ for $L = 2.5$, 7, 10 mm, respectively. The second characteristic time point $t_2 = 0.154$, 0.153 s and the corresponding total potential energy $W_2 = 2.26$ and 2.27 mJ for $L = 7$, 10 mm, respectively. From Fig. 10 it also can be seen that the maximum value of W and the time to reach it increase with the increase of the half specimen width L, consequently the number of crack levels and the length of the longest crack increase with the increase of L.

4.3. Effectiveness of the periodic model

Finally we discuss the effectiveness of the present periodic model. A comparison of the present periodic model and random models[34,38] with experiments is shown in Fig. 11. As seen in Fig. 11(a), the thermal shock cracks predicted by the present model show strict periodic patterns, whereas the experimental photographs exhibit some degree of dispersity. Fig. 11(b) shows the numerical simulations by non-local failure model.[34] The model abandoned the periodic assumption of crack patterns and considered the end boundary effects. Fig. 11(c) shows the numerical simulations by gradient damage model.[38] The model did not adopt any a priori hypotheses on cracks geometry. Apparently the random models can simulate random disturbance and are closer to real thermal shock crack patterns, which improves

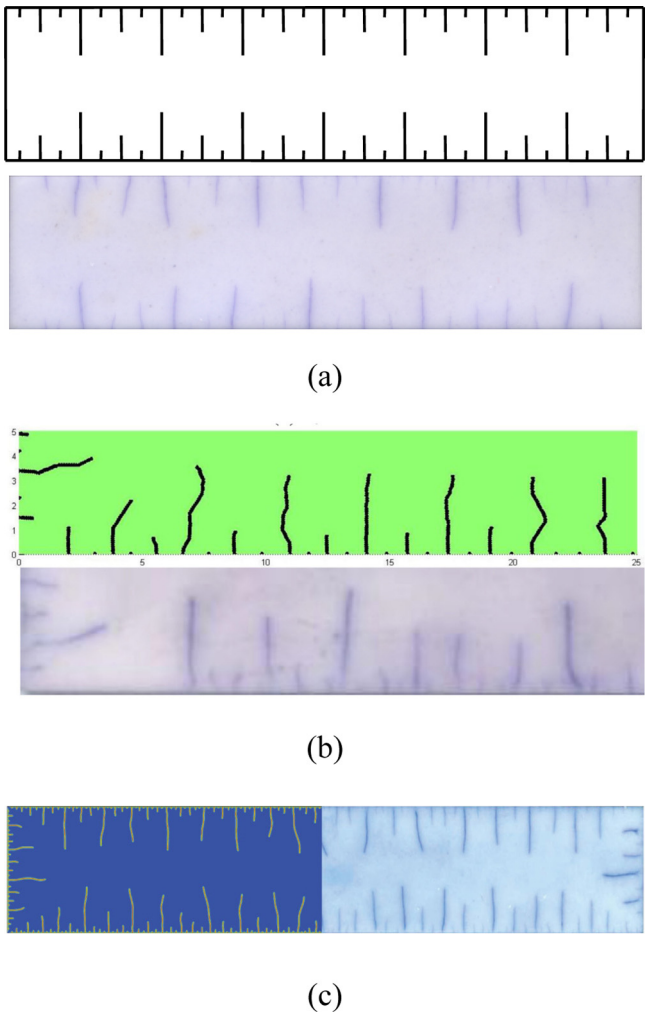

Fig. 11. A comparison of the periodic and random models with experiments: (a) present periodic model simulation; (b) non-local fracture model simulation;[34] (c) gradient damage model simulation.[38]

the scientific understanding of the formation of thermal shock crack patterns. It is noted that the random models predicted a key feature: the formation of periodic crack patterns. The periodic model can capture the essential feature of thermal shock crack patterns while greatly reduce computational cost. In other words, the periodic and random models verify and complement each other.

5. Conclusions

(1) A set of water-quenching experiments on thin ceramic specimens at various preset temperatures and for various values of the specimen width yielded elegant two-dimensional readings of thermal shock crack patterns. It was observed that the crack length distribution exhibited elegant periodic and hierarchical characteristics at every preset temperature and for every specimen width. The hierarchical number of the crack length and the crack length of the longest level showed an increasing trend with the increase of the specimen width. The spacing of the cracks of the longest level increased with the increase of specimen width, while the spacing of all the cracks was independent of specimen width. The fluctuation in the average crack spacing in eight specimens at every preset temperature and for every specimen width was small.

(2) At present, accurate data of the effective convective heat transfer coefficients at high temperatures are unavailable. In this work they were inversely estimated from the crack spacing data provided by experiments. The present experiments showed that the effective convective heat transfer coefficients were independent of the specimen size. Such a founding may help engineers to assess the thermal shock failure of practical components by designing specimens of standard size, which will greatly reduce experimental cost.

(3) Based on the minimum potential energy principle, numerical simulations were developed to investigate the evolution of crack patterns during the thermal shock process. The crack patterns predicted by the numerical simulations have strict periodic and hierarchical characteristics. According to the predicted ratio of the crack number of various levels, we classified experimental statistical results of the thermal shock cracks and found that the numerical predictions are in good agreement with experimental results.

(4) The driving force of thermal shock crack propagation is provided by the total potential energy. It was found that before the cracks of the longest level propagate alone, the total potential energy can be regarded as size-independent. This fact implies a theoretical inference that except the cracks of the longest level, the crack lengths of various levels and the corresponding starting propagation time should be size-independent. The theoretical inference was verified by experimental data.

It is concluded that the theoretical and numerical studies not only reproduce the evolution of crack patterns during the thermal shock process, but also reveal the essential laws governing the process, which will greatly improve the scientific understanding of thermal shock cracking phenomenon and promote applications of ceramics in thermal engineering.

Acknowledgements

This work was supported by the National Natural Science Foundation of China (Grants nos. 11172023, 11232013, 11472285 and 11302009), the Fundamental Research Funds for the Central Universities and funding from the French ANR program T-Shock ANR-10-INTB-0915.

References

1. Padture NP, Gell M, Jordan EH. Thermal barrier coatings for gas-turbine engine applications. *Science* 2002;**296**:280–4.
2. Kingery WD. Factors affecting thermal stress resistance of ceramic materials. *J Am Ceram Soc* 1955;**38**(1):3–15.
3. Hasselman DPH. Elastic energy at fracture and surface energy as design criteria for thermal shock. *J Am Ceram Soc* 1963;**46**(11):535–40.
4. Hasselman DPH. Unified theory of thermal shock fracture initiation and crack propagation in brittle ceramics. *J Am Ceram Soc* 1969;**52**(11):600–4.
5. Lu TJ, Fleck NA. The thermal shock resistance of solids. *Acta Mater* 1998;**46**(13):4755–68.

6. Collin M, Rowcliffe D. Analysis and prediction of thermal shock in brittle materials. *Acta Mater* 2000;**48**(8):1655–65.
7. Singh JP, Tree Y, Hasselman DPH. Effect of bath and specimen temperature on the thermal stress resistance of brittle ceramics subjected to thermal quenching. *J Mater Sci* 1981;**16**(8):2109–18.
8. Absi J, Glandus JC. Improved method for severe thermal shocks testing of ceramics by water quenching. *J Eur Ceram Soc* 2004;**24**(9):2835–8.
9. Hugot F, Glandus JC. Thermal shock of alumina by compressed air cooling. *J Eur Ceram Soc* 2007;**27**(4):1919–25.
10. Yuan C, Vandeperre LJ, Stearn RJ, Clegg WJ. The effect of porosity in thermal shock. *J Mater Sci* 2008;**43**(12):4099–106.
11. Shao YF, Du RQ, Wu XF, Song F, Xu XH, Jiang CP. Effect of porosity on the crack pattern and residual strength of ceramics after quenching. *J Mater Sci* 2013;**48**(18):6431–6.
12. Tomba AG, Cavalieri AL. Alumina disks with different surface finish: thermal shock behavior. *J Eur Ceram Soc* 2000;**20**(7):889–93.
13. Hasselman DPH. Strength behavior of polycrystalline alumina subjected to thermal shock. *J Am Ceram Soc* 1970;**53**(9):490–5.
14. Becher PF, Lewis D, Carman KR, Gonzalez. Thermal shock resistance of ceramics: size and geometry effects in quench tests. *Ceram Bull* 1980;**59**(5):542–8.
15. Becher PF. Effect of water bath temperature on the thermal shock of Al_2O_3. *J Am Ceram Soc* 1981;**64**(1):C17–8.
16. Cotterell B, Ong SW, Qin CD. Thermal shock and size effects in castable refractories. *J Am Ceram Soc* 1995;**78**(8):2056–64.
17. Sherman D, Schlumm D. Thickness effect in thermal shock of alumina ceramics. *Scripta Mater* 2000;**42**(8):819–25.
18. Gupta TK. Effect of specimen size on the strength degradation of Al_2O_3 subject to thermal shock. *J Am Ceram Soc* 1975;**58**(3-4):158–9.
19. Mai YW. Thermal-shock resistance and fracture-strength behavior of two tool carbides. *J Am Ceram Soc* 1976;**59**(11-12):491–4.
20. Glandus JC, Boch P. Influence of the size factor on the thermal shock resistance of ceramic samples. *Int J Thermophys* 1981;**2**(1):89–101.
21. She JH, Ohji T, Deng ZY. Thermal shock behavior of porous silicon carbide ceramics. *J Am Ceram Soc* 2002;**85**(8):2125–7.
22. Ding SQ, Zeng YP, Jiang DL. Thermal shock resistance of in situ reaction bonded porous silicon carbide ceramics. *Mater Sci Eng A* 2006;**425**(1-2):326–9.
23. Bažant ZP, Ohtsubo H, Aoh K. Stability and post-critical growth of a system of cooling or shrinkage cracks. *Int J Fract* 1979;**15**(5):443–56.
24. Nemat-Nasser S. Stability of a system of interacting cracks. *J Int Eng Sci* 1978;**16**(4):277–85.
25. Nemat-Nasser S, Keer LM, Parihar KS. Unstable growth of thermally induced interacting cracks in brittle solids. *Int J Solids Struct* 1978;**14**(6):409–30.
26. Bahr HA, Fischer G, Weiss HJ. Thermal-shock crack patterns explained by single and multiple crack propagation. *J Mater Sci* 1986;**21**(8):2716–20.
27. Bahr HA, Balke H, Kuna M, Liesk H. Fracture analysis of a single edge cracked strip under thermal shock. *Theor Appl Fract Mech* 1987;**8**(1):33–9.
28. Bahr HA, Weiss HJ, Maschke HG, Meissner F. Multiple crack propagation in a strip caused by thermal shock. *Theor Appl Fract Mech* 1988;**10**(3):219–26.
29. Jenkins DR. Optimal spacing and penetration of cracks in a shrinking slab. *Phys Rev E: Stat Nonlinear Soft Matter Phys* 2005;**71**(5):056117.
30. Choules BD, Kokini K, Taylor TA. Thermal fracture of ceramic thermal barrier coatings under high heat flux with time-dependent behavior: Part 1. Experimental results. *Mater Sci Eng A* 2001;**299**(1-2):296–304.
31. Kim Y, Lee WJ, Case ED. The measurement of the surface heat transfer coefficient for ceramics quenched into a water bath. *Mater Sci Eng A* 1991;**145**(1):L7–11.
32. Lee WJ, Kim Y, Case ED. The effect of quenching media on the heat transfer coefficient of polycrystalline alumina. *J Mater Sci* 1993;**28**(8):2079–83.
33. Jiang CP, Wu XF, Li J, Song F, Shao YF, Xu XH, et al. A study of the mechanism of formation and numerical simulations of crack patterns in ceramics subjected to thermal shock. *Acta Mater* 2012;**60**(11):4540–50.
34. Li J, Song F, Jiang CP. Direct numerical simulations on crack formation in ceramic materials under thermal shock by using a non-local fracture model. *J Eur Ceram Soc* 2013;**33**(13–14):2677–87.
35. Francfort GA, Marigo JJ. Revisiting brittle fracture as an energy minimization problem. *J Mech Phys Solids* 1998;**46**(8):1319–42.
36. Bourdin B, Francfort GA, Marigo JJ. The variational approach to fracture. *J Elast* 2008;**91**(1–3):5–148.
37. Bourdin B, Maurini C, Knepley M. Numerical simulation of reservoir stimulation—a variational approach. In: *Proceedings, thirty-sixth workshop on geothermal reservoir engineering*. 2011.
38. Bourdin B, Marigo JJ, Maurini C, Sicsic P. Morphogenesis and propagation of complex cracks induced by thermal shocks. *Phys Rev Lett* 2014;**112**:014301.
39. Sicsic P, Marigo JJ, Maurini C. Initiation of a periodic array of cracks in the thermal shock problem: a gradient damage modeling. *J Mech Phys Solids* 2014;**63**(2):256–84.
40. Cyron CJ, Marigo JJ, Sicsic P. Cohesive model approach to the nucleation and propagation of cracks due to a thermal shock. *Int J Fract* 2014;**187**(1):51–75.
41. Touloukian YS, Ho CY. *Thermophysical properties of matter. Thermal conductivity of nonmetallic solids*, 2. New York, NY: Plenum Press; 1972.
42. Touloukian YS, Ho CY. *Thermophysical properties of matter. Specific heat of nonmetallic solids*, 5. New York, NY: Plenum Press; 1972.
43. Jiang DL, Li LT, Ouyang SHX, Shi JL. *China materials engineering canon*. Beijing: Chemical Industry Press; 2006 (in Chinese).